SCIENTIFIC REPORTS

Quantum Capacitance in Topological Insulators

SUBJECT AREAS:
MAGNETIC MATERIALS AND DEVICES
APPLIED PHYSICS
MATERIALS PHYSICS
ELECTRONIC MATERIALS AND DEVICES

Received
30 May 2012

Accepted
22 August 2012

Published
18 September 2012

Correspondence and requests for materials should be addressed to F.X. (Faxian@iastate.edu) or K.L.W. (wang@ee.ucla.edu)

Faxian Xiu[1], Nicholas Meyer[1], Xufeng Kou[2], Liang He[2], Murong Lang[2], Yong Wang[3], Xinxin Yu[2], Alexei V. Fedorov[4], Jin Zou[5] & Kang L. Wang[2]

[1]Department of Electrical and Computer Engineering, Iowa State University, Ames, USA, [2]Department of Electrical Engineering, University of California, Los Angeles, California 90095, USA, [3]State Key Laboratory of Silicon Materials and Center for Electron Microscopy, Department of Materials Science and Engineering, Zhejiang University, Hangzhou, 310027, China, [4]Advanced Light Source Division, Lawrence Berkeley National Laboratory, 1 Cyclotron Road, Berkeley, California, 94720, USA, [5]Materials Engineering and Centre for Microcopy and Microanalysis, The University of Queensland, Brisbane QLD 4072, Australia.

Topological insulators show unique properties resulting from massless, Dirac-like surface states that are protected by time-reversal symmetry. Theory predicts that the surface states exhibit a quantum spin Hall effect with counter-propagating electrons carrying opposite spins in the absence of an external magnetic field. However, to date, the revelation of these states through conventional transport measurements remains a significant challenge owing to the predominance of bulk carriers. Here, we report on an experimental observation of Shubnikov-de Haas oscillations in quantum capacitance measurements, which originate from topological helical states. Unlike the traditional transport approach, the quantum capacitance measurements are remarkably alleviated from bulk interference at high excitation frequencies, thus enabling a distinction between the surface and bulk. We also demonstrate easy access to the surface states at relatively high temperatures up to 60 K. Our approach may eventually facilitate an exciting exploration of exotic topological properties at room temperature.

In recent years, the discovery of a new class of topological states of matter, known as time-reversal invariant Z_2 topological insulators (TIs), has generated considerable excitement in condensed matter physics. These materials are characterized by a bulk insulating energy gap and gapless edges or surface states which are topologically protected because an electron's spin is locked to its momentum due to a strong spin-orbit interaction[1–14]. Theory predicts that the unique surface states hosting Dirac fermions are robust and immune to defects, non-magnetic impurities and other perturbing influences in their environment, leading to potential non-dissipative applications[3,14–16]. To experimentally determine the macroscopic properties of the Dirac fermions and intentionally gain a control of the helical states, substantial efforts have been made in improving material quality using topological thin films[17–22], bulk crystals[5,13,23] and nanostructures[24–26] and in developing sensitive approaches for revealing surface transport and spin textures using angle-resolved photoemission (ARPES)[6,13,17,21,27,28], scanning tunneling microscopy (STM)[8,29], low-temperature transport[5,23,30–33], and optical polarizations[10]. While significant progress has been achieved in identifying Dirac fermions via Shubnikov-de Haas (SdH) oscillations[5,31] and ambipolar field effects[30] at low temperatures, experimental realization of exotic new physical phenomena arising from the surface states has been hindered by parallel bulk conductions due to naturally occurring defects and residual carrier doping[13,21,28]. Thus, developing new methods of separating the contributions from the bulk and surface states becomes one of the most important tasks in the field, particularly in the high temperature regime where bulk carriers are activated[25].

Quantum capacitance has advantages over traditional transport measurements because it allows us to directly probe the surface density of states (DOS), whereas the latter are more complicated and sensitive to scattering details[34]. Quantum capacitance is described by the equation $C_Q = e^2 D(E)$, where $D(E)$ represents the DOS[34–36]. Thus, a simple measurement of quantum capacitance provides a quantitative description of the DOS at the Fermi energy[34,36–43]. Despite its capability of directly probing electronic compressibility at high temperatures[34], this concept has never been applied to TIs, which is in part attributed to the lack of high-quality crystals, on which a large atomically flat surface is required for detectable quantum capacitance. As the material quality has been progressively improved recently[5,17,18,21–24,30–32,44], the quantum capacitance measurements become especially important as they can potentially solve today's intriguing challenge of high-temperature surface-state detection and may subsequently lead to the exploration of quantized anomalous and quantum spin Hall effects[1,14–16,45].

Here, we report on an observation of quantum capacitance using a topological capacitor device fabricated on Bi_2Se_3 thin films. Under external magnetic fields, by varying gate voltages, we observed pronounced capacitance oscillations associated with the creation of quantized Landau levels. Remarkably, by changing the *ac* frequency during the measurements, the amplitudes of the oscillations can be systematically tuned. As a result, high-frequency excitations are observed to sufficiently resolve the surface states up to 60 K. Our theoretical simulations further suggest that the different frequency responses of carriers from the surface and bulk states may account for the distinction of the surface states at high frequencies.

Results

Growth of Bi_2Se_3 thin films. Bi_2Se_3 thin films were grown on Si (111) substrates using an ultra-high vacuum molecular-beam epitaxy (MBE) system. Figure 1**a** presents a large-scale atomic force microscopy (AFM) image of an as-grown Bi_2Se_3 film with a thickness of 10 nm, exhibiting terraces over 500 nm in size. The surface consists of triangle-shaped terraces and steps (~1 nm in height, Supplementary Fig. S1), indicative of a hexagonal crystal structure along the (111) direction[18]. Real-time reflection high-energy electron diffraction (RHEED) was used to monitor the *in-situ* growth dynamics with the electron beam incident to the $[11\bar{2}0]$direction. The sharp streaky lines indicate a 2D growth mode and a flat surface morphology (Fig. 1**b**). To verify the existence of the surface states, high-resolution ARPES experiments along the $\overrightarrow{\Gamma}-\overrightarrow{K}$direction were performed at 64 K (Fig. 1**c**). A nearly linear *E-k* dispersion is observed near the Dirac point. The inset presents a curvature analysis of the raw data for a clear visualization of the band dispersion. The Fermi level is located ~0.4 eV above the Dirac cone, suggesting a very high bulk concentration. Such a large binding energy of the Dirac point in the Bi_2Se_3 thin film is believed to originate from the creation of Se vacancies by Se out-diffusion[22,31,46] during the pre-annealing process, as the film was annealed at 200°C for 2 hours before the ARPES experiments. Other widely observed effects such as band bending[22,31,47] and photoemission-induced gating[48] may not play significant roles in our film because of the large bulk density after annealing. The surface states must also be examined via other techniques such as low-temperature transport and STM, where a heating process and period can be minimized during sample preparation. As anticipated, the transport experiments exhibit clear SdH oscillations (Supplementary Fig. S2). Unlike the ARPES results, the Fermi level was estimated to be 53±5 meV above the Dirac point, consistent with the value of 70±20 meV obtained from the STM experiments (Supplementary Fig. S3). The location of the Fermi level relative to the Dirac point can be further verified using the quantum capacitance measurements, as discussed later.

Capacitor device structure. To perform accurate capacitance measurements, an appropriate design of the device structure is essential. Capacitance measurements are extremely intricate because they involve multiple components that respond to different frequencies. To minimize the undesired components, the structure of the devices must be as simple as possible. Figure 1**d** presents a schematic drawing of a capacitor using a 10 nm-thick Bi_2Se_3 thin film as the channel layer. A metal stack of Fe/Al (20/100 nm) is deposited on the top surface of the Bi_2Se_3 thin film to act as the source and drain contacts. A thin layer of Al_2O_3 (15 nm) is used as the gate oxide.

The total gate capacitance (C_T) can be modeled as a series of oxide capacitance (C_{OX}), quantum capacitance (C_Q), depletion/accumulation capacitances ($C_{D/A}$), and bulk capacitance (C_B), that is, $1/C_T=1/C_{OX}+1/C_Q+1/C_{D/A}+1/C_B$. Note that there are other parasitic capacitances associated with the source and drain; however, by performing a measurement on a device with identical geometry but without the topological insulator channel, these parasitic capacitances are negligible compared with the top-gate capacitance. To a first approximation, we may thus neglect the effect due to the parasitic capacitances. The total gate capacitance is primarily dominated by the smallest capacitance component in the system, *i.e.*, the smallest magnitude among C_{OX}, C_Q, $C_{D/A}$ and C_B. To gain further insight into the underlying physics, the concepts of C_Q and $C_{D/A}$ must be clarified. C_Q represents the quantum capacitance associated with the topological surface DOS, while $C_{D/A}$ describes a depletion (C_D) or an

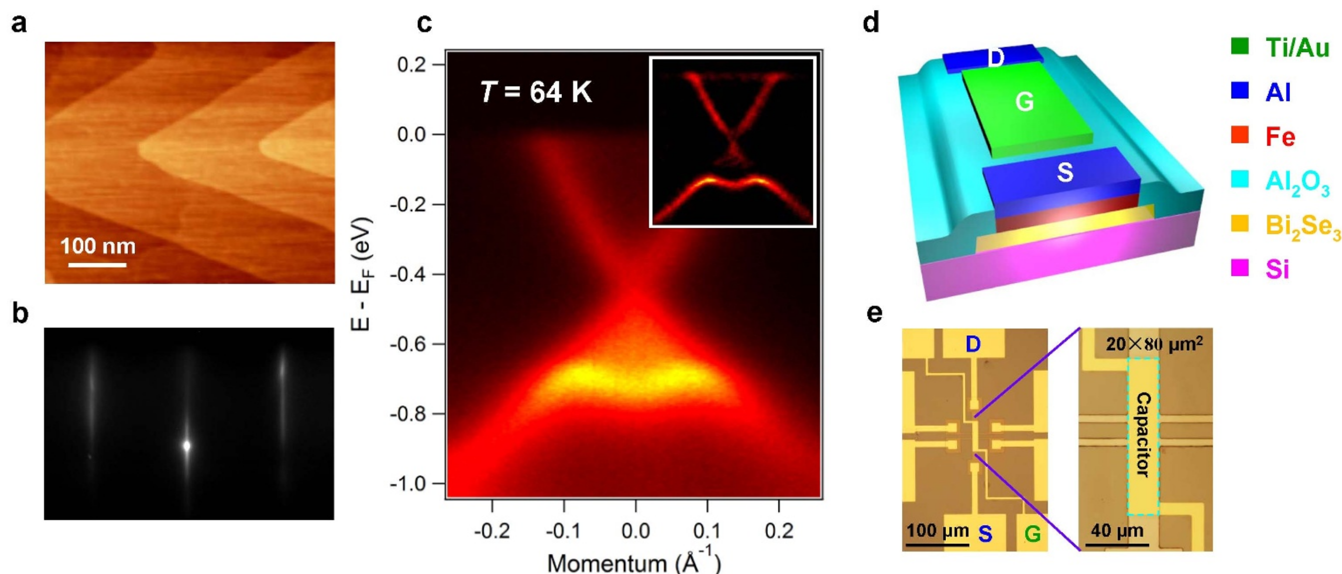

Figure 1 | Bi_2Se_3 growth, an ARPES spectrum and a topological capacitor device. (a) An AFM image of an MBE-grown Bi_2Se_3 thin film with terrace size exceeding 500 nm. (b) A streaky RHEED pattern along the $[11\bar{2}0]$ direction of the as-grown surface of Bi_2Se_3, indicating a 2-D growth mode. (c) An ARPES spectrum of the film along the $\overrightarrow{\Gamma}-\overrightarrow{K}$direction at T=64 K. The inset shows the curvature of the raw data for better visualization of the band dispersion. The Fermi Level lies ~0.4 eV above the Dirac point. (d) A capacitor device consisting of a 10 nm-thick Bi_2Se_3 thin film as the channel layer. The source-drain contacts were composed of Fe/Al (20 nm/100 nm), while the gate electrode consists of Ti/Au, 10 nm/100 nm. (e) An optical microscope image of the capacitor device structure. The effective area of the capacitor approaches 1600 μm², which enables a precise detection of quantum capacitance from the Bi_2Se_3 top surface.

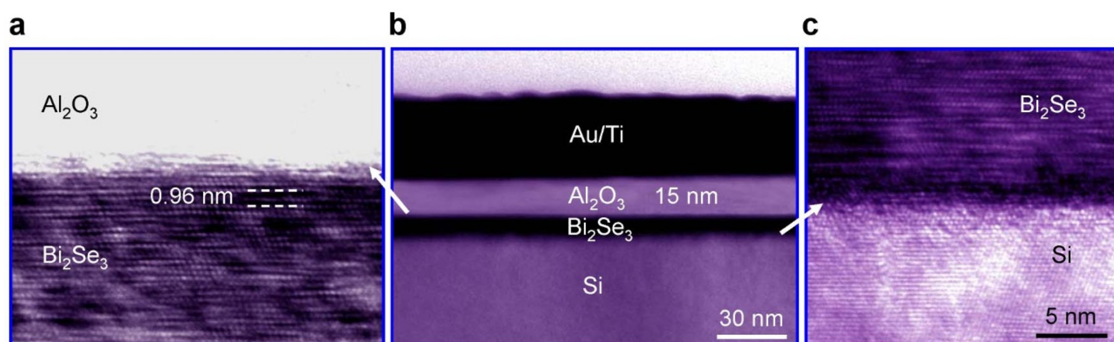

Figure 2 | Cross-section TEM images of a Bi_2Se_3 capacitor device. (a) A high-resolution TEM picture of the top surface of Bi_2Se_3 with a thickness of approximately10 nm. Al_2O_3–Bi_2Se_3 has an atomically sharp interface, which helps to preserve the topological states. The lattice spacing between the (0003) planes is measured to be 0.96 nm. (b) A low-magnification TEM image of the entire cross-section structure of the Bi_2Se_3 capacitor device. A thin and high-quality Al_2O_3 film of 15 nm is used to increase the oxide capacitance, making it possible to observe quantum capacitance from the Bi_2Se_3 top surface. (c) A high-resolution TEM for the bottom interface between Bi_2Se_3 and Si. An atomically sharp interface is also observed.

accumulation capacitance (C_A) during device operation. Under a depletion mode, electrons are depleted within a depth of w. Depending on the applied voltage, the depletion capacitance C_D changes its magnitude owing to the dynamic variation of w (ref. 49). Thus, in this scenario, a direct comparison of the magnitude of the different capacitive components is challenging without constructing numerical simulation models. However, in contrast, under an accumulation mode, the capacitance C_A becomes much larger than the other components. In particular, as the gate bias increases, a steady rise of the carrier density produces a large C_A according to the equation $C_A = (\varepsilon_{TI}/\sqrt{2}\lambda_n)(N_S/N_D)^{1/2}$(refs. 37,49,50), where ε_{TI} is the dielectric constant of Bi_2Se_3, λ_n is the extrinsic Debye length, N_s is the carrier density in the inversion layer and N_D is the density of ionized donors. Consequently, as the device enters a saturation regime, the total capacitance can be simplified as $1/C_T = 1/C_{OX} + 1/C_Q + 1/C_B$ with the bulk capacitance C_B being an unknown parameter. By systematically increasing the measurement frequency, the C_B component can be easily eliminated based upon different frequency response of the surface and bulk carriers[49,51–54], as elaborated in the Simulation and Discussion section. Therefore, the extraction of C_Q becomes immediately feasible under the accumulation mode, where the oxide capacitance can be calculated by $C_{OX} = \varepsilon_r \varepsilon_0 / d$ (d is the thickness of Al_2O_3).

Figure 1**e** shows an optical microscope image of the capacitor device structure. We performed the Hall and capacitance measurements with a Hall bar geometry. The effective area of the capacitor is measured to be approximately 1600 μm^2. The large area ensures a high signal-to-noise ratio and a good estimation of the quantum capacitance from the Bi_2Se_3 top surface. The cross-section of the practical Hall bar devices was examined using a high-resolution transmission electron microscopy (HRTEM). As illustrated in Fig. 2**b**, the device consists of 15 nm of Al_2O_3 and 10 nm of Bi_2Se_3. The interfaces at the top and bottom of the Bi_2Se_3 thin film both have atomically sharp heterojunctions (Fig. 2**a** and 2**c**). The lattice spacing is observed to be 0.96 nm, consistent with other reports[18,24].

Quantum capacitance in Bi_2Se_3 thin films. Figure 3 plots the total capacitance as a function of gate voltage, magnetic field and

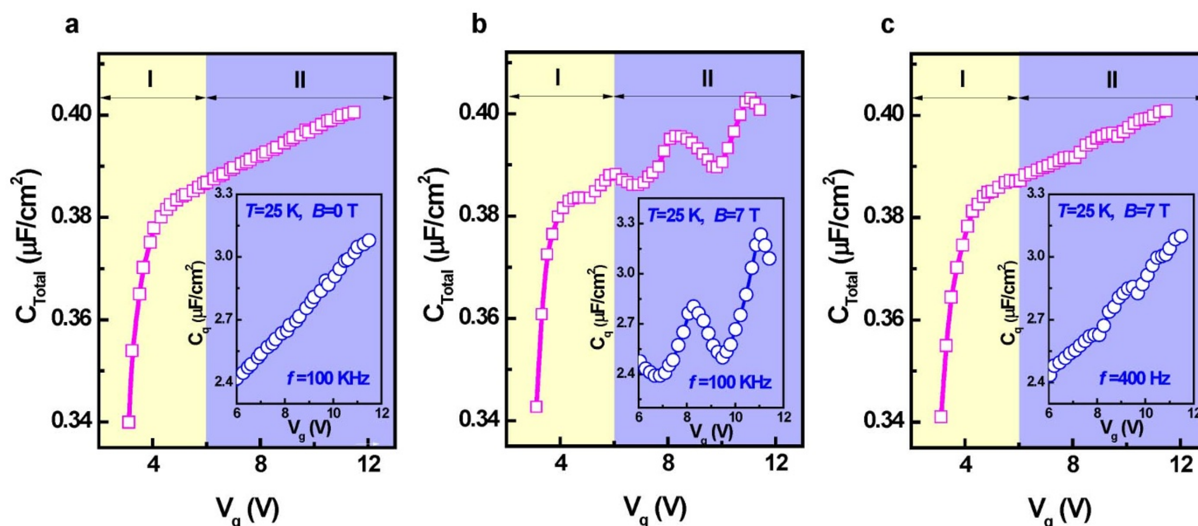

Figure 3 | Extraction of quantum capacitance in Bi_2Se_3 capacitors. (a) The total capacitance as a function of gate voltage at $T=25$ K, $B=0$ T and $f=100$ KHz. The capacitance values in regimes I (yellow) and II (light purple) are dominated by the bulk and the TI top surface, respectively. The continuing increase in the total capacitance in regime II suggests the presence of quantum capacitance (C_Q), which can be directly extracted based on a series capacitor model where $1/C_T = 1/C_{OX} + 1/C_Q$. The resultant C_Q is shown in the inset. (b) The total capacitance as a function of gate voltage at $T=25$ K, $B=7$ T and $f=100$ KHz. Capacitance oscillations were observed under an external magnetic field of 7 T, suggesting the creation of Landau levels from the surface states. The inset presents the extracted oscillatory C_Q. (c) The total capacitance as a function of gate voltage at $T=25$ K, $B=7$ T and $f=400$ Hz. As compared with (b) under low-frequency excitation, the quantum oscillations tend to diminish. These results indicate that detection of the surface states can be achieved by applying high frequencies during the C-V measurements.

measurement frequency in a Bi_2Se_3 capacitor at 25 K. In general, two regimes are observed for the gate voltage ranging from 0 to 12 V. In regime I, the total capacitance is dominated by the depletion capacitance; however, the quantum capacitance cannot be extracted because of the uncertainty of the depletion component[49]. When the gate voltage further increases, the total capacitance tends to saturate (Fig. 3**a** and 3**c**), the quantum capacitance not only contributes a small correction to the total gate capacitance but also begins to dominate over the other components in this regime. The system can be then simplified as $1/C_T=1/C_{OX}+1/C_Q$ (the term C_B is eliminated at high frequencies as shown in Fig. 4); here, the oxide capacitance is calculated to be 0.46 μF/cm² by taking $d = 15$ nm and $\varepsilon_r=7.8$ (extracted from the control sample, Supplementary Fig. S4).

For a traditional MOS capacitor, under the accumulation mode, the capacitance should saturate at a constant value corresponding to the oxide capacitance (Supplementary Fig. S4, a regular MOS capacitor without Bi_2Se_3). For a Bi_2Se_3 capacitor, however, the total capacitance increases continuously as the gate scans from 6 to 12 V (Fig. 3**a**). The gradual increase of the total capacitance must originate from an additional capacitive component (Supplementary Fig. S5), which could be attributed to the quantum capacitance of the surface states. To verify this presumption, we applied a magnetic field of 7 T perpendicular to the sample surface to observe the possible quantization of Landau levels. Indeed, significant capacitance oscillations were resolved (Fig. 3**b**), suggesting that the quantum capacitance becomes dominant and changes significantly with varying gate voltage and magnetic field[34]. It is speculated that during the capacitance-voltage (*C-V*) measurements, the Fermi level is shifted because of the gating effect[33]: as it moves across each discrete Landau level, the quantum capacitance becomes oscillatory (Fig. 3**b** inset, C_Q vs. V_g). This analysis is essentially the same as for the case of SdH oscillations (R_{xx} vs. *B*, where R_{xx} represents longitudinal resistance)[42,55], and the capacitance results are nearly identical to the transport measurements but with a much higher temperature. By subtracting the oxide capacitance, C_Q from the topological surface is retrieved, as depicted in all three insets of Fig. 3. The obtained C_Q is on the order of 2 μF/cm², reasonably near the theoretical calculation (Supplementary Fig. S5). To explore the effect of frequency on the surface states, the excitation frequency was reduced from 100 KHz to 400 Hz. The quantum oscillations, however, diminished rapidly, exhibiting a noisy spectrum without evident traces of oscillations (Fig. 3**c** inset). These observations imply that the detection of the surface states can be achieved by applying high frequency excitations during the *C-V* measurements.

Figure 4 shows a comprehensive analysis of the quantum capacitance in Bi_2Se_3 for different experimental settings. Figure 4**a** demonstrates the magnetic field dependence of the total capacitance at 100 KHz and 25 K. When the magnetic field increases from 3 to 9 T, the low-index Landau levels with large interleave spacing progressively move across the Fermi level, reminiscent of typical SdH oscillations from transport measurements[42,55] (see also Supplementary Fig. S2). Figure 4**b** demonstrates a clear trend of frequency-dependent quantum oscillations, where high frequency excitations resolve the surface oscillations quite well. Figures 4(**e**,**f**) and 4(**i**,**j**) present similar results but at higher temperatures of 35 and 50 K, respectively. Note that the frequency can have a significant effect on the distinction of the surface from the bulk[49,51–54], presumably because of the dramatic difference in carrier mobility: in the bulk, the electron mobility is approximately 380 cm²/V s, while on the surface the electron mobility reaches over 10,000 cm²/V s (Supplementary Figs. S2 and S6). Such a large difference enables a fast response from the surface states, analogous to the fast response of high-mobility electrons in graphene (in a gigahertz range)[56]; as a comparison, the bulk carriers cannot follow the high frequency excitations, resulting in a "filtering" effect[49,51]. More importantly, the surface states can be clearly distinguished at approximately 60 K (Fig. 4**c** and Supplementary Fig. S7), much beyond the capability of the low-temperature transport, where movable carriers travel along horizontal channels and are extremely sensitive to bulk properties (scattering details)[34]. In addition, quantum capacitance probes both the extended and localized states, whereas electron transport can only investigate the former one[34].

To better understand the physics behind this phenomenon, we performed a quantitative analysis of the SdH oscillations. Figure 4**c** demonstrates the temperature dependence of the total capacitance when the magnetic field and frequency are set to 7 T and 100 KHz, respectively. The surface states are persistent up to 60 K. Three peaks are identified, corresponding to the generation of three Landau levels in the system. The first derivative of the total capacitance was also taken to remove the background parasitic capacitances (Fig. 4**d**). The three peaks from P1 to P3 have a common 90° phase shift compared with those in Fig. 4**c**. Now, we can take the amplitude of the capacitance oscillations − note that the Al_2O_3 capacitance C_{OX} is removed − and apply$\Delta C(T)/\Delta C(0)=\lambda(T)/\sinh(\lambda(T))$, where the thermal factor is given by$\lambda(T)=2\pi^2 k_B T m_{cycl}/(\hbar eB)$(refs. 5,23). Here, m_{cycl} denotes the cyclotron mass, k_B is Boltzmann's constant, and $\hbar$ is the reduced Plank's constant. By taking the conductivity oscillation amplitude and performing the best fit to the equation of $\Delta C(T)/\Delta C(0)$ (Fig. 4**g**), m_{cycl} is calculated to be 0.079 m_0, 0.091 m_0, and 0.102 m_0 at gate voltages of 5.9 V (P1), 8 V (P2) and 10.9 V (P3), respectively (Fig. 4**g** (inset)). These values are reasonably close to those extracted from the transport measurements (0.07 m_0, Supplementary Fig. S2). Here, m_0 is the electron rest mass. Because the cyclotron mass is given by $m_{cycl}=E_F/V_F^2$(ref. 5), where E_F and V_F are the Fermi level and the Fermi velocity, both E_F and V_F can be precisely obtained given $m_{cycl}V_F=\hbar k_F$(ref. 23). It is noted that the Fermi level increases from 61.5 to 79.4 meV when the gate voltage is varied from +5.9 to +10.9 V (Fig. 4**h**), exhibiting the clear gate modulation behavior of the surface states. The k_F value can also be obtained in the range of 0.025–0.033 Å^{-1}, consistent with the transport results (Supplementary Fig. S2).

We performed a series of sample rotations under a constant magnetic field of 7 T to identify the nature of the quantum oscillations (Fig. 4**k** and 4**i**)[5,23]. As the system is rotated from 0 to 50°, the amplitude of the oscillations dampens and the oscillation frequency (peak interval) changes, depending on the magnitude of $B_\perp$(Fig. 4**k** inset), which signifies the typical 2-D characteristics of the topological surface states[5]. The relationship between the carrier density n and the Fermi vector k_F is the same for both quadratic (2-DEG) and linear (TI surface state) *E-k* dispersion relations and is given by $n\propto k_F^2/\pi$(refs. 39,57). Accordingly, the period of SdH oscillations for both 2-DEG and TI surface states also exhibit similar behavior given the Onsager relation of $f=1/\Delta(1/B)=2\hbar\pi n/q$(ref. 5). Therefore, it is difficult to distinguish the surface states from 2-DEG through the conventional magneto-transport measurements, which can only probe the carriers that transport through the channel. However, unlike the transport approach, the quantum capacitance method can circumvent this challenge by providing a direct extraction of an important quantity, dn/dV_a (ref. 39, V_a − the voltage dropped on the TI surface), which explicitly describes the surface states. By carefully examining their *E-k* relations and DOS[39,57], *i.e.*, $E(k)=\hbar v_F|k|$ & $g_{TI}(E)=g|E|/2\pi(\hbar v_F)^2$ for the surface states, $E(k)=\hbar^2 k^2/2m$ & $g_{2DEG}(E)=mN(E)/\pi\hbar^2$ for 2-DEG, one can theoretically derive and simulate their capacitances, as demonstrated in Supplementary Figs. S5 and S8. Here, $g=g_s g_v$ is the degeneracy factor, considering both the spin and energy band degeneracies for the TI surface states. The quantum capacitance associated with the surface states strongly depends on the density of states, similar to that of graphene[34,36,37]. By contrast, for 2-DEG the capacitance is saturated at a constant value irrespective of the change in V_a (Supplementary Fig. S8). Therefore, the observed quantum oscillations in Figs. 3 and 4 are attributed to the surface states instead of 2-DEG, which is also

Figure 4 | Quantitative analysis of quantum capacitance in Bi_2Se_3. (a, b) Magnetic-field- and frequency-dependent capacitance at T=25 K and f=100 KHz. (e, f) and (i, j) The same measurements when the temperature is increased to 35 and 50 K, respectively. C_Q demonstrates a strong frequency dependence at all three temperatures. (c) Temperature-dependent capacitance at B=7 T and f=100 KHz. Three oscillation peaks are clearly identified, denoted as P1, P2 and P3. (d) The first derivative of the total capacitance as a function of temperature. P1, P2 and P3 correspond to the three valleys of the peaks because of a 90° phase shift compared with those in (c). (g) Extraction of the cyclotron effective mass by taking the temperature-dependent oscillation amplitude in (d). Three effective masses for peaks P1–P3 were obtained in the inset. (h) Fermi vector k_F and Fermi energy E_F as a function of gate voltage. The inset describes the calculated positions of the Fermi level relative to the Dirac point. (k) The total capacitance as a function of the measurement angles. The inset depicts the measurement setup, in which the device was rotated from 0 to 50°. (i) The first derivative of the total capacitance as a function of the rotation angle. The traces of arrows (in purple) and dots (in green) suggest the change of the oscillation frequencies. The curves in all the figures except for (g), (h) and (k) are vertically shifted for clarity.

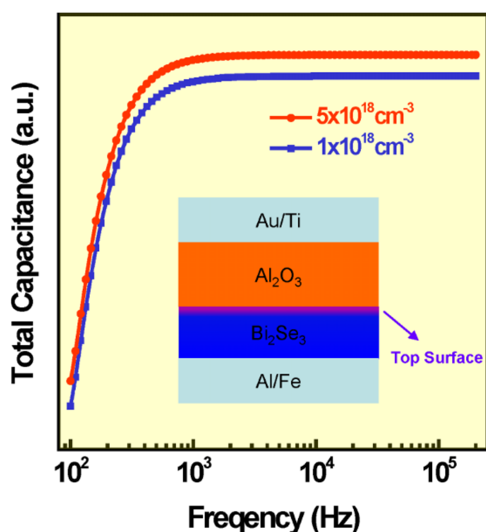

Figure 5 | Simulated frequency-dependent total capacitance. A device model from the inset is constructed in accordance with the experimental setup (Figs. 1**d** and 1**e**). During simulations, only the top surface of Bi_2Se_3 is considered. At low frequencies, the total capacitance exhibits a strong dependence on frequency, primarily attributed to the sufficient responses for the bulk and the surface carriers. When the frequency is set beyond 1 KHz, however, a desirable surface-dominant regime is attained, in which the bulk interference is reduced at elevated frequencies. The inset depicts the device structure used for the simulations.

verified by an ambipolar field effect in quantum capacitance (Supplementary Fig. S11).

Discussion

To understand the frequency dependence of quantum oscillations, we carried out qualitative simulations using Technology Computer Aided Design (TCAD). A capacitor device was constructed by considering the experimental conditions. Figure 5 shows that the total capacitance changes with the frequency of the *ac* signals. In essence, the capacitance for the system depends on the total available charges under specific measurement frequencies[49,51]. In the low-frequency regime ($f <$ 1 KHz, Fig. 5), both the bulk and surface carriers can respond to the external *ac* signals, and the system can be represented by a series capacitor model ($1/C_T = 1/C_{OX} + 1/C_Q + 1/C_B$). The bulk interference exists in the system, and the quantum capacitance can hardly make itself distinguishable. In the high-frequency regime ($f >$ 1 KHz, Fig. 5), however, the available charges accounting for the total capacitance primarily originate from the surface states because the bulk carriers do not have adequate time to respond to the high *ac* frequencies[51–54]. Thus, the elimination of the bulk term leads to a significant manifestation of the surface quantum capacitance ($1/C_T = 1/C_{OX} + 1/C_Q$). By taking two different surface carrier densities (Fig. 5, red and blue curves), we can verify the effect of the available surface charges on the total capacitance. In short, our simulations provide sensible explanations for the observed frequency dispersion of the total capacitance, although a detailed theoretical treatise is still needed. The discovery of the quantum capacitance in topological insulators may facilitate future progress toward the creation of topological devices by probing high-temperature surface states and incorporating gated structures.

Methods

MBE growth. Thin film growth was carried out with an ultra-high vacuum Perkin Elmer MBE system. Si (111) substrates were cleaned using the standard Radio Corporation of America (RCA) procedure before being transferred into the growth chamber. High-purity Bi (99.9999%) and Se (99.99%) elementary sources were evaporated by conventional effusion cells. During growth, the Bi and Se cells were kept at 490 and 200°C, respectively, while the Si (111) substrate was kept at 150°C (growth temperature). The epitaxial growth was monitored using the *in-situ* RHEED technique, and the surface was observed to be atomically flat, as evidenced by the streaky RHEED patterns (Fig. 1**a**). Digital images of the RHEED were captured using a KSA400 system made by K-space Associate, Inc.

Characterizations. (1) **ARPES.** High-resolution ARPES experiments were performed at beam line 12.0.1 of the Advanced Light Source at Lawrence Berkeley National Laboratory, using 100 eV and 52 eV photons to measure the core levels and surface states, respectively. (2) **TEM.** High-resolution TEM experiments were performed on a Philips Tecnai F20 (S)TEM operating at 200 KV. The digital images were recorded by a Gatan® 2k×2k CCD camera. (3) **Capacitance measurements.** Frequency-dependent capacitance measurements were conducted with an HP/Agilent 4274A multi-frequency LCR meter. The *ac* frequency could be tuned from 100 Hz–100 KHz, while a *dc* bias can be applied from 0 to ± 35 V. The LCR meter was connected to a physical property measurement system (PPMS), where the devices were located. We were also able to systematically vary several experimental variables such as the temperature, magnetic field, measurement frequency, and external gate bias. Multiple lock-in-amplifiers and Keithley source meters were also connected to the PPMS system, enabling comprehensive and high-sensitivity transport measurements for the top-gated Hall bar and capacitor devices.

Device fabrication. The MBE-grown Bi_2Se_3 thin film (~10 nm) was patterned into a micron-scale Hall bar geometry using conventional optical photolithography and a subsequent CHF_3 dry-etching of 18 s. A 15-nm-thick, high-κ Al_2O_3 dielectric layer was deposited using atomic layer deposition (ALD). Hall channel contacts were defined by *e*-beam evaporation after etching away Al_2O_3 in the contact areas. A metal stack of Fe/Al (20 nm/100 nm) was directly deposited onto the exposed Bi_2Se_3 surface. A top-gate metal scheme of Ti/Au (10 nm/90 nm) was achieved using a second step of photolithography and *e*-beam evaporation.

Device simulation. We used a visual TCAD software package (version 1.7.3) from Cogenda.com. The simulated device structure is depicted in Fig. 5 inset. The topological surface is assumed to have a depth of 1 nm and carrier densities of 1×10^{18} cm^{-3} and 5×10^{18} cm^{-3} (two scenarios). Bulk Bi_2Se_3 has a carrier density of 6.5×10^{19}–1.3×10^{20} cm^{-3}, attributed to the formation of an impurity band as elaborated in Supplementary Fig. S6. Our simplified model describes the physics of frequency-dependent capacitance in a qualitative manner. The absolute values of the total capacitance can be varied by altering the above parameters; however, the underlying physics remains the same, which forms the basis of our simulations.

1. Kane, C. L. & Mele, E. J. Topological order and the quantum spin Hall effect. *Phys. Rev. Lett.* **95**, 146802 (2005).
2. Zhang, H. *et al.* Topological insulators in Bi_2Se_3, Bi_2Te_3 and Sb_2Te_3 with a single Dirac cone on the surface. *Nat. Phys.* **5**, 438–442 (2009).
3. Moore, J. Topological insulators: The next generation. *Nat. Phys.* **5**, 378–380 (2009).
4. Fu, L. & Kane, C. L. Topological insulators with inversion symmetry. *Phys. Rev. B* **76**, 045302 (2007).
5. Qu, D.-X., Hor, Y. S., Xiong, J., Cava, R. J. & Ong, N. P. Quantum oscillations and Hall anomaly of surface states in the topological insulator Bi_2Te_3. *Science* **329**, 821–824 (2010).
6. Xia, Y. *et al.* Observation of a large-gap topological-insulator class with a single Dirac cone on the surface. *Nat. Phys.* **5**, 398–402 (2009).
7. Zhang, T. *et al.* Experimental demonstration of topological surface states protected by time-reversal symmetry. *Phys. Rev. Lett.* **103**, 266803 (2009).
8. Alpichshev, Z. *et al.* STM imaging of electronic waves on the surface of Bi_2Te_3:topologically protected surface states and hexagonal warping effects. *Phys. Rev. Lett.* **104**, 016401 (2010).
9. Veldhorst, M. *et al.* Josephson supercurrent through a topological insulator surface state. *Nat Mater* advance online publication (2012).
10. McIver, J. W., Hsieh, D., Steinberg, H., Jarillo Herrero, P. & Gedik, N. Control over topological insulator photocurrents with light polarization. *Nat Nano* **7**, 96–100 (2012).
11. Cho, S. *et al.* Topological insulator quantum dot with tunable barriers. *Nano Letters* **12**, 469–472 (2012).
12. Bahramy, M. S., Yang, B. J., Arita, R. & Nagaosa, N. Emergence of non-centrosymmetric topological insulating phase in BiTeI under pressure. *Nat Commun* **3**, 679 (2012).
13. Arakane, T. *et al.* Tunable Dirac cone in the topological insulator Bi2-xSbxTe3-ySey. *Nat Commun* **3**, 636 (2012).
14. Qi, X. L., Hughes, T. L. & Zhang, S. C. Topological field theory of time-reversal invariant insulators. *Phys. Rev. B* **78**, 195424 (2008).
15. Bernevig, B. A., Hughes, T. L. & Zhang, S.-C. Quantum spin Hall effect and topological phase transition in HgTe quantum wells. *Science* **314**, 1757–1761 (2006).
16. Konig, M. *et al.* Quantum spin hall insulator state in HgTe quantum wells. *Science* **318**, 766–770 (2007).
17. Zhang, Y. *et al.* Crossover of the three-dimensional topological insulator Bi_2Se_3 to the two-dimensional limit. *Nat. Phys.* **6**, 584–588 (2010).

18. Kou, X. F. *et al.* Epitaxial growth of high mobility Bi_2Se_3 thin films on CdS. *Appl. Phys. Lett.* **98**, 242102 (2011).
19. Bansal, N. *et al.* Epitaxial growth of topological insulator Bi2Se3 film on Si(111) with atomically sharp interface. *Thin Solid Films* **520**, 224–229 (2011).
20. Li, H. D. *et al.* The van der Waals epitaxy of Bi_2Se_3 on the vicinal Si(111) surface: an approach for preparing high-quality thin films of a topological insulator. *New Journal of Physics* **12**, 103038 (2010).
21. Zhang, J. *et al.* Band structure engineering in $(Bi_{1-x}Sb_x)_2Te_3$ ternary topological insulators. *Nat Commun* **2**, 574 (2011).
22. Brahlek, M., Kim, Y. S., Bansal, N., Edrey, E. & Oh, S. Surface versus bulk state in topological insulator Bi_2Se_3 under environmental disorder. *Appl. Phys. Lett.* **99**, 012109 (2011).
23. Taskin, A. A., Ren, Z., Sasaki, S., Segawa, K. & Ando, Y. Observation of Dirac Holes and Electrons in a Topological Insulator. *Phys. Rev. Lett.* **107** (2011).
24. Kong, D. & Cui, Y. Opportunities in chemistry and materials science for topological insulators and their nanostructures. *Nat Chem* **3**, 845–849 (2011).
25. Xiu, F. Manipulating surface states in topological insulator nanoribbons. *Nature Nanotech.* **6**, 216–221 (2011).
26. Peng, H. *et al.* Topological insulator nanostructures for near-infrared transparent flexible electrodes. *Nat Chem* advance online publication (2012).
27. Chen, Y. L. *et al.* Massive Dirac Fermion on the Surface of a Magnetically Doped Topological Insulator. *Science* **329**, 659–662 (2010).
28. Bianchi, M. *et al.* Coexistence of the topological state and a two-dimensional electron gas on the surface of Bi2Se3. *Nat Commun* **1**, 128 (2010).
29. Cheng, P. *et al.* Landau quantization of topological surface states in Bi_2Se_3. *Phys. Rev. Lett.* **105**, 076801 (2010).
30. Steinberg, H., Gardner, D. R., Lee, Y. S. & Jarillo-Herrero, P. Surface State Transport and Ambipolar Electric Field Effect in Bi_2Se_3 Nanodevices. *Nano Letters* **10**, 5032–5036 (2010).
31. Analytis, J. G. *et al.* Two-dimensional surface state in the quantum limit of a topological insulator. *Nat. Phys.* **6**, 960–964 (2010).
32. Sacépé, B. *et al.* Gate-tuned normal and superconducting transport at the surface of a topological insulator. *Nat Commun* **2**, 575 (2011).
33. Chen, J. *et al.* Gate-Voltage Control of Chemical Potential and Weak Antilocalization in Bi_2Se_3. *Phys. Rev. Lett.* **105**, 176602 (2010).
34. Ponomarenko, L. A. *et al.* Density of States and Zero Landau Level Probed through Capacitance of Graphene. *Phys. Rev. Lett.* **105**, 136801 (2010).
35. Luryi, S. Quantum capacitance devices. *Appl. Phys. Lett.* **52**, 501–503 (1988).
36. Xu, H. *et al.* Quantum Capacitance Limited Vertical Scaling of Graphene Field-Effect Transistor. *ACS Nano* **5**, 2340–2347 (2011).
37. Xia, J., Chen, F., Li, J. & Tao, N. Measurement of the quantum capacitance of graphene. *Nat Nano* **4**, 505–509 (2009).
38. Ilani, S., Donev, L. A. K., Kindermann, M. & McEuen, P. L. Measurement of the quantum capacitance of interacting electrons in carbon nanotubes. *Nat Phys* **2**, 687–691 (2006).
39. John, D. L., Castro, L. C. & Pulfrey, D. L. Quantum capacitance in nanoscale device modeling. *J. Appl. Phys.* **96**, 5180–5184 (2004).
40. Giannazzo, F., Sonde, S., Raineri, V. & Rimini, E. Screening Length and Quantum Capacitance in Graphene by Scanning Probe Microscopy. *Nano Letters* **9**, 23–29 (2008).
41. Guo, J., Yoon, Y. & Ouyang, Y. Gate Electrostatics and Quantum Capacitance of Graphene Nanoribbons. *Nano Letters* **7**, 1935–1940 (2007).
42. Henriksen, E. A. & Eisenstein, J. P. Measurement of the electronic compressibility of bilayer graphene. *Phys. Rev. B* **82**, 041412 (2010).
43. Droscher, S. *et al.* Quantum capacitance and density of states of graphene. *Appl. Phys. Lett.* **96**, 152104 (2010).
44. Cho, S., Butch, N. P., Paglione, J. & Fuhrer, M. S. Insulating Behavior in Ultrathin Bismuth Selenide Field Effect Transistors. *Nano Letters* **11**, 1925–1927 (2011).
45. Yu, R. *et al.* Quantized Anomalous Hall Effect in Magnetic Topological Insulators. *Science* **329**, 61–64 (2010).
46. Kim, Y. S. *et al.* Thickness-dependent bulk properties and weak antilocalization effect in topological insulator Bi_{2}Se_{3}. *Phys. Rev. B* **84**, 073109 (2011).
47. Hsieh, D. *et al.* A tunable topological insulator in the spin helical Dirac transport regime. *Nature* **460**, 1101–1105 (2009).
48. Kordyuk, A. A. *et al.* Photoemission-induced gating of topological insulators. *Phys. Rev. B* **83**, 081303 (2011).
49. Sze, S. *Physics of Semiconductor Devices*, 3rd ed. (Wiley, New York, 2007).
50. Lind, E., Niquet, Y.-M., Mera, H. & Wernersson, L.-E. Accumulation capacitance of narrow band gap metal-oxide-semiconductor capacitors. *Appl. Phys. Lett.* **96**, 233507 (2010).
51. Bülbül, M. M. & Zeyrek, S. Frequency dependent capacitance and conductance–voltage characteristics of Al/Si_3N_4/p-Si(100) MIS diodes. *Microelectronic Engineering* **83**, 2522–2526 (2006).
52. Lieneweg, U. Frequency response of charge transfer in MOS inversion layers. *Solid-State Electronics* **23**, 577–583 (1980).
53. Xuan, Y., Lin, H. C., Ye, P. D. & Wilk, G. D. Capacitance-voltage studies on enhancement-mode InGaAs metal-oxide-semiconductor field-effect transistor using atomic-layer-deposited Al[sub 2]O[sub 3] gate dielectric. *Appl. Phys. Lett.* **88**, 263518 (2006).
54. Jiang, J., Awadelkarim, O. O., Lee, D. O., Roman, P. & Ruzyllo, J. On the capacitance of metal/high-k dielectric material stack/silicon structures. *Solid-State Electronics* **46**, 1991–1995 (2002).
55. Zhang, Y., Tan, Y.-W., Stormer, H. L. & Kim, P. Experimental observation of the quantum Hall effect and Berry's phase in graphene. *Nature* **438**, 201–204 (2005).
56. Liao, L. *et al.* High-speed graphene transistors with a self-aligned nanowire gate. *Nature* **467**, 305-308 (2010).
57. Fang, T., Konar, A., Xing, H. & Jena, D. Carrier statistics and quantum capacitance of graphene sheets and ribbons. *Appl. Phys. Lett.* **91**, 092109 (2007).

Acknowledgements

F.X. would like to acknowledge the financial support received from the National Science Foundation under the Award No. 1201883, and the College of Engineering at Iowa State University. The Microelectronics Research Center at Iowa State provided substantial equipment supports during the project. F.X., K.W. Y.W. and J.Z. would like to thank the Focus Center Research Program-Center on Functional Engineered Nano Architectonics (FENA), the Australia Research Council. Y.W. would like to thank National Science Foundation of China (No. 11174244) for the financial support received for this project. F.X. would like to acknowledge Mingqiang Bao for setting up the CV measurement system, Peng Zhang for helpful discussions on ARPES, and Shen Chen for extensive guidance on the usage of the Visual TCAD software.

Author contributions

F.X. conceived and designed the research. F.X., X.K. and M.L. fabricated the capacitor devices and performed the measurements. L.H., M.L. and X.Y. contributed to the measurements and analysis. Y.W. and J.Z. performed structural analysis. A.V. provided the ARPES measurements. X.K. and F.X. performed numerical simulations on capacitances. F.X., N.M. and X.K. wrote the paper, with help from all the other co-authors.

Additional information

Reprints and permission information is available online at http://npg.nature.com/reprintsandpermissions.

Supplementary information accompanies this paper at http://www.nature.com/scientificreports

Competing financial interests: The authors declare no competing financial interests.

License: This work is licensed under a Creative Commons Attribution-NonCommercial-ShareAlike 3.0 Unported License. To view a copy of this license, visit http://creativecommons.org/licenses/by-nc-sa/3.0/

How to cite this article: Xiu, F. *et al.* Quantum Capacitance in Topological Insulators. *Sci. Rep.* **2**, 669; DOI:10.1038/srep00669 (2012).